Article

*Discovery Medicine* 2026; 38(204): 215–228
https://doi.org/10.24976/Discov.Med.202638204.17

# The MIB2-CYLD Axis Impairs Osteogenic-Angiogenic Coupling via Ubiquitination-Mediated Oxidative Stress

Chao Shi[1], Xin Xi[2], Yue Xiong[2,3], Liang Peng[1,4], Zheqing An[1,2], Rui Luo[5], Yuting Cheng[2,3], Jian Liao[2,3,*]

[1]School of Clinical Medicine, Guizhou Medical University, 550004 Guiyang, Guizhou, China
[2]School/Hospital of Stomatology, Guizhou Medical University, 550004 Guiyang, Guizhou, China
[3]Key Laboratory of Oral Disease Research, Guizhou Medical University, 550004 Guiyang, Guizhou, China
[4]Department of Orthopedics, The First People's Hospital of Guiyang, 550002 Guiyang, Guizhou, China
[5]Department of Orthopedics, Guizhou Provincial People's Hospital, 550002 Guiyang, Guizhou, China
*Correspondence: liaojian@gmc.edu.cn (Jian Liao)
Submitted: 30 October 2025 Revised: 2 December 2025 Accepted: 22 December 2025 Published: 20 January 2026

**Background: Osteogenic-angiogenic coupling is essential for skeletal homeostasis, and its dysregulation constitutes a pathological basis for osteoporosis. This study investigates whether the E3 ubiquitin ligase Mind bomb 2 (MIB2) plays a critical role in this coupling by regulating the deubiquitinase cylindromatosis (CYLD) and oxidative stress.**

**Methods: Key regulatory factors were identified using integrated bioinformatics analysis. Gain-of-function studies were performed on MC3T3-E1 osteoprogenitors and bEnd.3 endothelial cells through lentiviral transduction. Protein interactions and ubiquitination were assessed using co-immunoprecipitation and ubiquitination assays. Osteogenic differentiation and angiogenic capacity were evaluated by alkaline phosphatase activity assay, Alizarin Red S staining, scratch wound, and tube formation assays. Oxidative stress markers, including reactive oxygen species, malondialdehyde, and glutathione, were measured. Cellular crosstalk was examined using a Transwell co-culture system.**

**Results: CYLD was identified as a key node regulating both osteogenic and angiogenic processes. Functional studies demonstrated that CYLD overexpression enhanced osteogenic differentiation and angiogenesis while attenuating oxidative stress in both cell types. Mechanistically, MIB2 was identified as an E3 ubiquitin ligase for CYLD, binding CYLD and promoting its ubiquitination and degradation. Rescue experiments confirmed that MIB2 overexpression suppressed osteogenesis and induced oxidative stress (reactive oxygen species (ROS), reduced glutathione (GSH), and malondialdehyde (MDA)) by downregulating CYLD. Co-culture experiments further revealed that disruption of the MIB2–CYLD axis in osteoblasts significantly suppressed endothelial expression of key angiogenic markers (PECAM1, EMCN, and HIF-1$\alpha$), elevated intracellular ROS, and altered oxidative stress markers in the conditioned medium (GSH and MDA), thereby demonstrating that osteoblast-derived oxidative stress signals impair endothelial function and compromise osteogenic-angiogenic coupling.**

**Conclusion: MIB2 impairs osteogenic-angiogenic coupling through the ubiquitin-mediated degradation of CYLD, exacerbating oxidative stress and simultaneously suppressing osteogenesis and angiogenesis. These findings provide new insights into the pathogenesis of skeletal disorders and highlight the MIB2-CYLD axis as a potential therapeutic target.**

**Keywords:** MIB2; CYLD; oxidative stress; osteogenic differentiation; angiogenesis; osteogenic-angiogenic coupling

## Introduction

Bone is a dynamic organ that maintains locomotor function and metabolic homeostasis [1]. Its structural integrity depends on a delicate balance between osteoblast-mediated bone formation and osteoclast-driven bone resorption [2]. This equilibrium is critically supported by the coordinated process of osteogenic-angiogenic coupling [3]. The intraosseous vascular system not only delivers essential nutrients and oxygen to bone-metabolizing cells but also directly regulates osteogenic differentiation by secreting signaling molecules such as vascular endothelial growth factor and bone morphogenetic proteins [4]. In turn, osteoblast-derived factors, including platelet-derived growth factor and angiopoietin-1, promote endothelial cell proliferation, migration, and tubulogenesis, establishing a bidirectional regulatory circuit essential for osteogenic-angiogenic coupling [5]. Disruption of this coupling leads to bone loss, microarchitectural deterioration, and reduced vascular density, contributing to skeletal disorders such as osteoporosis (OP) and non-union fractures [6]. Therefore, elucidating the core regulatory mechanisms of osteogenic-angiogenic coupling and identifying key molecular targets are crucial for advancing the treatment of bone-related diseases.

Oxidative stress is a significant pathological driver of impaired osteogenic-angiogenic coupling [7]. Under

physiological conditions, low intracellular levels of reactive oxygen species (ROS) support processes such as osteogenic differentiation (e.g., by activating the transcription factor Runx2) and angiogenesis (e.g., by stabilizing hypoxia-inducible factor-1$\alpha$, HIF-1$\alpha$) [8]. However, under pathological states like aging, estrogen deficiency, or abnormal mechanical loading, excessive ROS accumulation disrupts cellular redox balance [9]. This oxidative burden inhibits osteoblast proliferation and differentiation while promoting apoptosis, partly through lipid peroxidation (e.g., elevated malondialdehyde, MDA) and protein oxidative damage [10]. Concurrently, it impairs endothelial tight junctions and vascular maturation, thereby disrupting the intraosseous vascular network [11]. For example, in an ovariectomized (OVX) osteoporotic rat model, ROS levels are markedly increased in bone tissue, accompanied by reduced vascular density and suppressed osteogenic markers [12]. Nevertheless, the key molecular pathways that regulate redox homeostasis in the bone microenvironment and sustain osteogenic-angiogenic coupling remain incompletely understood.

The ubiquitin (Ub)-proteasome system (UPS) serves as a central mechanism for maintaining protein homeostasis and modulating signaling pathways [13], with dysfunction associated to cancers, metabolic diseases, and skeletal disorders [14]. Within this system, E3 Ub ligases specifically recognize substrate proteins and catalyze Ub conjugation, whereas deubiquitinating enzymes (DUBs) counteract this process by removing Ub chains, thereby preserving substrate stability [15]. The dynamic balance between E3 Ub ligases and DUBs constitutes a precise regulatory network for protein turnover [16]. Tumor suppressor cylindromatosis (CYLD) is a conserved DUB that negatively regulates inflammatory responses and cell apoptosis by cleaving K63-linked Ub chains from substrates such as NF-$\kappa$B, p62, and JNK [17]. Accumulating evidence implicates CYLD in bone metabolism, as global knockout mice exhibit osteopenia due to enhanced osteoclast activity and impaired osteoblast function [18]. Although CYLD is shown to regulate angiogenesis and endothelial cell migration [19], its role in osteogenic-angiogenic coupling, especially in an oxidative stress-dependent context, remains unknown. Mind bomb 2 (MIB2), a HECT domain-containing E3 Ub ligase, is known to participate in embryonic development, immune cell differentiation, and tumor progression [20–22]. Moreover, MIB2 has been found to be essential for YAP/TAZ-dependent angiogenesis [23]. However, whether MIB2 influences bone metabolism, particularly via DUB targeting to regulate oxidative stress and osteogenic-angiogenic coupling, has not been explored.

To address these gaps, this study elucidates a novel mechanism by which MIB2-mediated ubiquitination of CYLD disrupts osteogenic-angiogenic coupling through oxidative stress, providing new theoretical and therapeutic insights into skeletal diseases.

## Materials and Methods

### *Bioinformatics Analysis*

Genes associated with osteogenic differentiation were derived from the OsteoporosAtlas database, a systematically curated collection of human osteoporosis-related genes as published by Wang *et al*. [24]. The gene list used in this study is provided in **Supplementary Table 1.**

Concurrently, factors related to oxidative stress and angiogenesis were screened using GeneCards (https://www.genecards.org/) with the search terms “oxidative stress” and “angiogenesis”. Deubiquitination-related genes were subsequently downloaded via UbiBrowser2.0 (http://ubibrowser.bio-it.cn/ubibrowser_v3/home/index). An intersection analysis was performed to identify overlapping genes among these datasets. Following this, UbiBrowser2.0 was employed to analyze and filter for regulatory factors associated with the intersecting genes.

### *Cell Culture and Transduction*

The mouse pre-osteoblastic cell line MC3T3-E1 (305187, Cytion, Eppelheim, Germany) and the mouse vascular endothelial cell line bEnd.3 (305265, Cytion) were cultured in MEM $\alpha$ medium (A1049001, Gibco™, Shanghai, China) supplemented with 10% fetal bovine serum (FBS) or in DMEM medium (820300a, Cytion), respectively. Both cell lines were authenticated by short tandem repeat (STR) profiling and confirmed to be free of interspecies contamination. The MC3T3-E1 cells exhibited a characteristic fibroblast-like, spindle-shaped morphology, while the bEnd.3 cells displayed a typical endothelial cobblestone-like morphology at confluence. Mycoplasma testing was performed for all cell lines, and results confirmed the absence of contamination (**Supplementary Fig. 1**). To investigate the functions of MIB2 and CYLD, lentiviral vectors for overexpressing human MIB2 (oe-MIB2; RefSeq: NM_001170687.4) and CYLD (oe-CYLD; RefSeq: NM_001378743.1), along with a corresponding empty vector control (oe-NC), were constructed by VectorBuilder. The full-length coding sequences were cloned under the control of the CMV promoter, with puromycin used as the selection marker. When cells reached 50–60% confluence, they were transduced with the lentiviral particles in the presence of 8 µg/mL polybrene to enhance transduction efficiency. The viral supernatant was replaced with fresh complete medium after 12 hours. To establish stable cell lines, puromycin selection (2 µg/mL) was initiated 48 hours post-transduction and maintained for 7 days. Gene and protein expression levels were assessed by quantitative polymerase chain reaction (qPCR) and Western blotting (WB), respectively. Additionally, intracellular levels of ROS, MDA, and reduced glutathione (GSH) were measured, as previously described [25].

### *Alkaline Phosphatase (ALP) Activity Assay*

MC3T3-E1 cells were seeded in 24-well plates at a density of $2 \times 10^4$ cells/well. Following transduction, cells were cultured for an additional 10 days in standard complete medium, which was replaced with fresh medium every two days. On day 10, cells were harvested and alkaline phosphatase (ALP) activity was evaluated using an ALP Assay kit (P0321S, Beyotime, Shanghai, China). Subsequently, ALP absorbance was measured at 405 nm using a microplate reader (BioTek Instruments Inc, Winooski, VT, USA).

### *Assessment of Osteogenic Differentiation and Mineralization*

MC3T3-E1 cells were seeded in 12-well plates at a density of $5 \times 10^4$ cells/well. To evaluate late-stage osteogenic mineralization capacity, calcium nodule formation was assessed using Alizarin Red S (ARS) staining. Transfected MC3T3-E1 cells were cultured in standard complete medium for 28 days, with the medium refreshed every three days. Upon completion of the culture period, the medium was aspirated and cells were gently rinsed twice with phosphate-buffered saline (PBS) (P2272, Sigma-Aldrich, Beijing, China). The cells were then fixed with 4% paraformaldehyde (158127, Sigma-Aldrich) for 30 minutes at room temperature. After fixation, an adequate volume of 0.5% ARS solution (pH 4.2, A5533, Sigma-Aldrich) was added to each well, followed by incubation at room temperature for 30 minutes in the dark. The staining solution was then removed, and cells were thoroughly washed with deionized water until the background became colorless. Mineralized nodules were visualized and imaged using an ECLIPSE Ts2R microscopy (Nikon, Tokyo, Japan). For semi-quantitative analysis, 10% cetylpyridinium chloride solution (C9002, Sigma-Aldrich) was added to solubilize the dye bound to calcium nodules with constant agitation. The resulting eluate was collected, and its absorbance was measured at a wavelength of 562 nm using a microplate reader.

### *Flow Cytometric Analysis of Intracellular Reactive Oxygen Species (ROS)*

Intracellular ROS levels were quantified using the cell-permeable fluorogenic probe 2′,7′-dichlorodihydrofluorescein diacetate (DCFH-DA). Harvested cells were washed with phosphate-buffered saline (PBS) and resuspended in serum-free medium containing 10 µM DCFH-DA (C400, Thermo Fisher Scientific). Cell suspensions were incubated at 37 ℃ for 30 minutes in the dark, with gentle mixing every 5–10 minutes. To remove excess extracellular probe, the cells were pelleted by centrifugation at 1000 ×g for 5 minutes at 4 ℃ and washed twice with ice-cold PBS. Finally, the cell pellet was resuspended in ice-cold PBS and kept on ice for immediate analysis. Flow cytometry was performed using a CytoFLEX flow cytometer (Beckman Coulter). For each sample, at least 10,000 singlet events, gated based on forward scatter (FSC) and side scatter (SSC) to exclude debris and aggregates, were acquired. The fluorescence of the oxidized product (dichlorofluorescein, DCF) was measured in the FITC channel (excitation/emission: 488/525 nm). Data were analyzed using CytExpert Software (Beckman Coulter, Indianapolis, IN, USA). The geometric mean fluorescence intensity (GeoMFI) of the DCF signal within the viable cell gate was recorded. To calculate the relative ROS level, the GeoMFI of each experimental sample was normalized to that of the corresponding control group, which was set as 1.0.

### *Colorimetric Detection of MDA and GSH Levels*

The levels of MDA and GSH in cell lysates or culture medium were measured using commercially available assay kits for MDA (S0131S, Beyotime) and GSH (CS0260, Sigma-Aldrich), respectively, following the manufacturers' protocols. For MDA detection, absorbance was measured at 532 nm, and the concentration was calculated using a standard curve of known MDA concentrations and normalized to the total protein content of each sample. For GSH detection, absorbance was measured at 412 nm, and the concentration was determined using a standard curve of known GSH concentrations and normalized to the total protein content. All absorbance measurements were performed using a microplate reader.

### *Reverse Transcription (RT)-qPCR*

Total RNA was isolated using TRI reagent® (T3934, Sigma-Aldrich) and treated with RNase-free deoxyribonuclease I (DNase I, AMPD1, Sigma-Aldrich) to eliminate genomic DNA contamination. RNA integrity was verified spectrophotometrically using an HD-UV90 system (Shandong Horde Electronic Technology Co., Ltd., Weifang, China) in strict accordance with the manufacturer's guidelines. For complementary DNA (cDNA) synthesis, 2 µg of total RNA was reverse-transcribed using the RevertAid RT kit (K1691, Thermo Fisher, Shanghai, China). RT-qPCR amplification was performed in 20 µL reaction volumes using a thermal cycler (QuantStudio 5 Real-Time PCR System; Applied Biosystems, CA, USA) with the following cycling parameters: initial denaturation at 95 °C for 10 minutes; 40 cycles of denaturation at 95 °C for 15 seconds, annealing at 60 °C for 30 seconds, and extension at 72 °C for 30 seconds. Target gene expression levels were normalized to the endogenous reference gene GAPDH, and relative mRNA expression was calculated using the $2^{-\Delta\Delta Ct}$ method. Primer sequences are listed in Table 1.

### *WB Analysis*

Proteins were extracted using RIPA lysis buffer (R0278, Sigma-Aldrich) via incubation on ice for 30 minutes, with brief vortexing at 5-minute intervals. Following

**Table 1. The primer sequences for RT-qPCR.**

| Gene | | Primer sequences (5′-3′) |
|---|---|---|
| *PECAM1* | Forward | CCAAAGCCAGTAGCATCATGGTC |
| | Reverse | GGATGGTGAAGTTGGCTACAGG |
| *EMCN* | Forward | GCACACACCATGTCACTGCTTC |
| | Reverse | CAGCGCGATAACCACAGGCAAA |
| *HIF-1α* | Forward | CCTGCACTGAATCAAGAGGTTGC |
| | Reverse | CCATCAGAAGGACTTGCTGGCT |
| *GAPDH* | Forward | CATCACTGCCACCCAGAAGACTG |
| | Reverse | ATGCCAGTGAGCTTCCCGTTCAG |

centrifugation of the cell lysates (12,000 rpm, 10 minutes, 4 ℃), the clarified supernatants were collected, and total protein concentration was determined using a bicinchoninic acid protein assay kit (BRK0011, ABclonal Technology, Wuhan, China). Equal amounts of protein were loaded and separated by sodium dodecyl sulfate-polyacrylamide gel electrophoresis, then transferred onto polyvinylidene fluoride membranes (88518, Thermo Fisher). The membranes were blocked with 5% skimmed milk for 1 hour, followed by incubation with the following primary antibodies at 4 ℃ overnight: CYLD (1:1000, 11110-1-AP, Proteintech, Wuhan, China), Runx2 (1:1000, 20700-1-AP, Proteintech), PECAM1 (1:1000, A19014, ABclonal Technology), EMCN (1:1000, 11828-1-AP, Proteintech), HIF-1$\alpha$ (1:20,000, ab179483, Abcam, Shanghai, China), MIB2 (1:1000, A17829, ABclonal Technology), and GAPDH (1:1000, 2118, Cell Signaling Technology, MA, USA). After washing, the membranes were incubated with a horseradish peroxidase-conjugated goat anti-rabbit IgG secondary antibody (1:10,000, 31460, Thermo Fisher) for 1 hour at room temperature. Protein bands were visualized using an enhanced chemiluminescence substrate (32106, Thermo Fisher), and band intensity was quantified densitometrically using ImageJ software (National Institutes of Health, Bethesda, MD, USA).

### *Scratch Wound Assay*

Cell migration was evaluated using a standardized scratch wound model in bEnd.3 cells. Cells were seeded in 12-well plates at a density of $8 \times 10^4$ cells/well and cultured until 100% confluent to form continuous monolayers. A uniform linear scratch was created in each monolayer using a sterile pipette tip, followed by washing to remove dislodged cellular debris. To minimize confounding effects associated with cell proliferation, the wounded monolayers were maintained in serum-free DMEM. Time-lapse imaging was performed at baseline (0 hour) and 24 hours after wounding using an ECLIPSE Ts2R microscopy. Acquired images were quantified with ImageJ software, and the migration rate was calculated.

### *Tube Formation Assay*

Matrigel matrix (356231, Corning, NY, USA) was applied to 96-well plates, which were subsequently incubated at 37 °C for 30 minutes to allow gel polymerization. Prepared endothelial cells were seeded in 96-well plates at a density of $1 \times 10^4$ cells/well onto the surface of the polymerized matrix. The plates were incubated at 37 °C under 5% $CO_2$ for 6 hours. Following incubation, images were acquired using an ECLIPSE Ts2R microscopy. Captured images were analyzed with ImageJ software to measure and quantify the total length of tubular structures, thereby assessing the angiogenic capability of the endothelial cells.

### *Co-IP*

Cells were collected and lysed using lysis buffer containing protease inhibitors, followed by incubation on ice for 30 minutes. After high-speed centrifugation to remove cellular debris, the supernatant was collected. To assess the physical interaction between MIB2 and CYLD, the supernatant was incubated overnight at 4 ℃ with an antibody against MIB2 (A17829, ABclonal Technology) or a control IgG antibody (SAB5600195, Sigma-Aldrich). Protein A/G magnetic beads (88802, Thermo Fisher) were then added and incubated for 2 hours to facilitate binding of the antibody-antigen complexes to the beads. The beads were washed three times, and the supernatant was removed by centrifugation. Loading buffer was added to the samples, which were then boiled for 5 minutes and subsequently subjected to WB analysis using an antibody against CYLD (11110-1-AP, Proteintech) to detect co-precipitated proteins.

### *Immunoprecipitation (IP)*

To assess the ubiquitination level of CYLD, stable mouse pre-osteoblastic MC3T3-E1 cells overexpressing MIB2 (oe-MIB2) or the corresponding empty vector control (oe-NC) were cultured until they reached 70–80% confluence. The cells were then treated with 10 μM of the proteasome inhibitor MG-132 (M8699, Sigma-Aldrich) for 4–6 hours to stabilize ubiquitinated proteins. After treatment, the cells were harvested and lysed. The cleared lysate was subjected to immunoprecipitation using an antibody against CYLD (11110-1-AP, Proteintech) overnight

at 4 °C, followed by incubation with Protein A/G magnetic beads. The immunoprecipitated complexes were washed extensively, eluted, and then analyzed by Western blotting. To specifically detect ubiquitinated CYLD, the membrane was probed with an anti-ubiquitin antibody (1:1000, 10201-2-AP, Proteintech). Parallel blotting for CYLD was performed to confirm equal precipitation.

### *Cycloheximide (CHX) Assay*

Cells from an appropriate cell line were cultured under standard conditions and allocated into control and experimental groups. The experimental group was transfected to overexpress MIB2. Cells in both groups were subsequently treated with 50 µg/mL cycloheximide (CHX) (C7698, Sigma-Aldrich) and harvested at specified time points (0, 0.5, 1, and 2 hours). The effect of MIB2 on CYLD protein stability was analyzed by WB.

### *Co-culture of MC3T3-E1 and bEnd.3 Cells*

This study employed a non-contact Transwell co-culture system to establish indirect paracrine interaction between mouse osteoprogenitor MC3T3-E1 cells and brain microvascular endothelial bEnd.3 cells. Transfected MC3T3-E1 cells were seeded in the upper chambers, while bEnd.3 cells were cultured in the lower compartments, allowing intercellular communication via soluble factors diffusing through the shared medium. After 48 hours of co-culture, both cell populations and conditioned media were separately collected for subsequent analyses.

### *Statistical Analysis*

All statistical analyses were performed using Prism 9 software (GraphPad Software, San Diego, CA, USA). Data were presented as mean ± standard deviation (SD). Comparisons between two groups were analyzed using Student's *t*-test. For comparisons across multiple groups, one-way or two-way analysis of variance (ANOVA) was applied as appropriate, followed by Tukey's post hoc test for multiple comparisons. A $p$-value of less than 0.05 was considered statistically significant.

## Results

### *CYLD Overexpression Promotes Osteoblastic Differentiation and Alleviates Oxidative Stress*

To identify key regulatory genes, we first retrieved osteogenic differentiation-related genes from the OsteoAtlas database, integrated oxidative stress and angiogenesis-related factors from GeneCards, and screened for DUBs using UbiBrowser 2.0. Intersection analysis identified CYLD as a candidate gene (Fig. 1A). To investigate its functional role, we overexpressed CYLD in MC3T3-E1 cells. WB analysis confirmed a marked increase in CYLD protein levels in the oe-CYLD group compared to the oe-NC control group ($p < 0.0001$, Fig. 1B). Functional assays demonstrated that CYLD overexpression significantly enhanced osteogenic differentiation, as evidenced by increased ALP activity ($p < 0.01$, Fig. 1C), elevated formation of mineralized nodules (Fig. 1D), and upregulation of Runx2 protein ($p < 0.01$, Fig. 1E). Regarding oxidative stress, cells overexpressing CYLD exhibited a substantial reduction in intracellular ROS ($p < 0.001$), accompanied by increased GSH content ($p < 0.001$) and decreased MDA levels ($p < 0.01$, Fig. 1F–H). Collectively, these findings indicate that CYLD not only promotes osteogenic differentiation but also helps maintain redox homeostasis in osteoblastic cells.

### *CYLD Overexpression Enhances Angiogenic Capacity in Endothelial Cells*

To further investigate the functional impact of CYLD on angiogenesis, we overexpressed CYLD in bEnd.3 endothelial cells. WB analysis confirmed a significant increase in CYLD expression in the oe-CYLD group compared to the oe-NC control group ($p < 0.01$, Fig. 2A). Functional assays revealed that CYLD upregulation markedly enhanced cellular migration, as demonstrated by improved scratch wound closure, and potentiated the capacity for tubular structure formation *in vitro* ($p < 0.001$, Fig. 2B,C). At the molecular level, RT-qPCR and WB analyses showed that CYLD overexpression significantly upregulated both mRNA and protein expression of key angiogenesis-related markers, including PECAM1, EMCN, and HIF-1$\alpha$ ($p < 0.01$, Fig. 2D,E). Concurrently, endothelial cells overexpressing CYLD exhibited substantially reduced intracellular levels of ROS ($p < 0.001$) and MDA ($p < 0.01$), alongside increased GSH content ($p < 0.001$, Fig. 2F–H). These collective results indicate that CYLD enhances angiogenic function and ameliorates the cellular oxidative stress status in endothelial cells.

### *MIB2 Functions as an E3 Ub Ligase Targeting CYLD for Degradation*

To elucidate the upstream regulatory mechanism of CYLD, we analyzed the UbiBrowser 2.0 database and identified MIB2 as a candidate E3 Ub ligase potentially targeting CYLD (Fig. 3A). To validate whether MIB2 acts as the E3 Ub ligase for CYLD, we overexpressed MIB2 in MC3T3-E1 cells. WB analysis revealed that CYLD protein levels were significantly reduced upon MIB2 upregulation ($p < 0.05$, Fig. 3B). Co-IP experiments confirmed a direct interaction between MIB2 and CYLD within cells (Fig. 3C). Further ubiquitination assays demonstrated that MIB2 overexpression enhanced the ubiquitination level of CYLD (Fig. 3D). To substantiate the effect of MIB2 on CYLD protein stability, cells were treated with the protein synthesis inhibitor CHX. The results showed an accelerated degradation rate of CYLD protein in MIB2-overexpressing cells ($p < 0.01$, Fig. 3E). These data indicate that MIB2 binds to CYLD and promotes its ubiquitination and proteasomal degradation, suggesting that MIB2 functions as an E3 Ub ligase for CYLD.

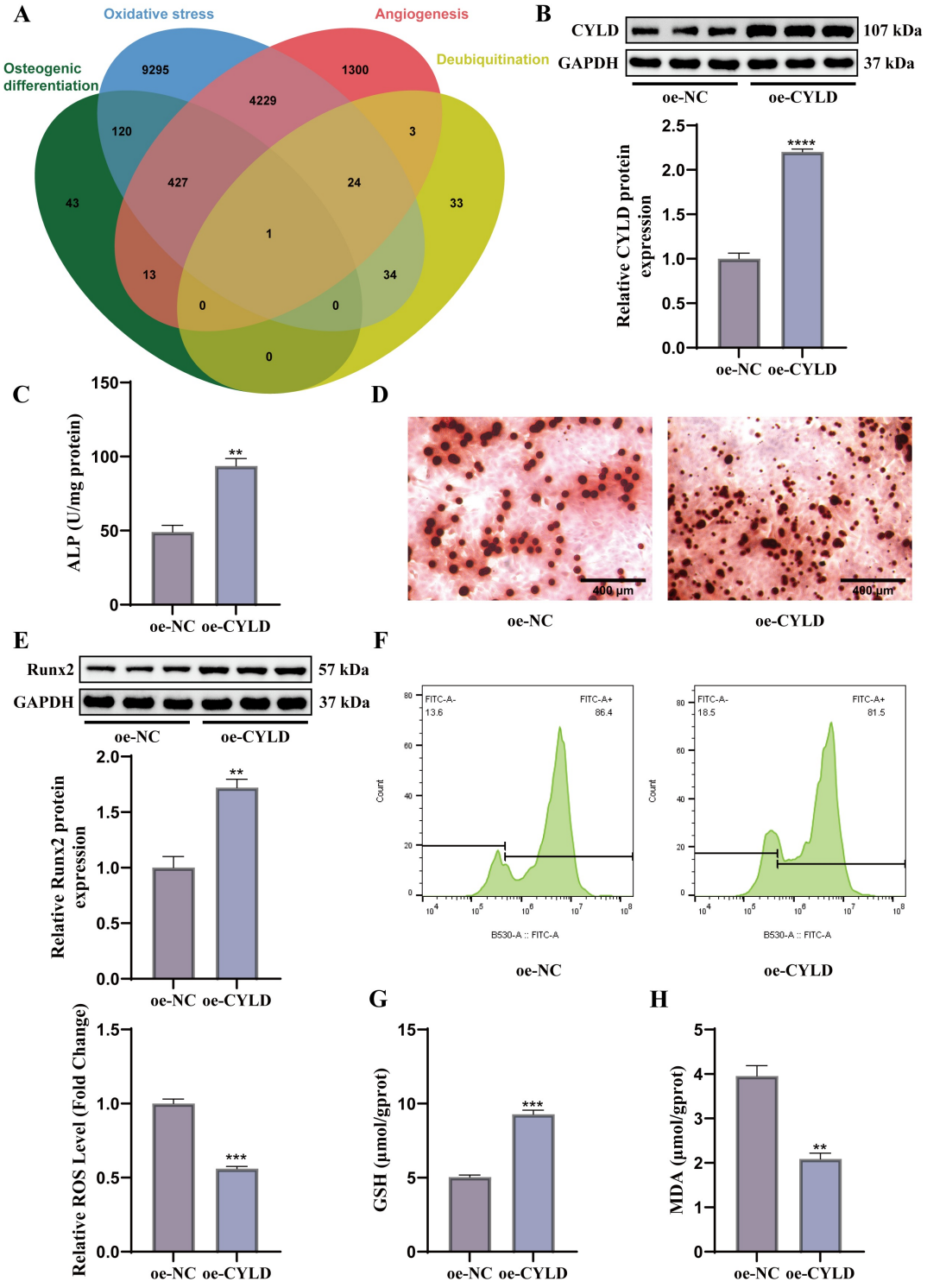


**Fig. 1. CYLD overexpression promotes osteoblastic differentiation and alleviates oxidative stress.** (A) Venn diagram of the intersection analysis among genes related to osteogenic differentiation, oxidative stress, angiogenesis, and deubiquitination. (B) WB of CYLD protein expression in MC3T3-E1 cells. (C) ALP activity assay. (D) Alizarin Red S staining of mineralized nodules. (E) WB of Runx2 protein expression in MC3T3-E1 cells. (F) Relative intracellular ROS level, determined as the fold change in geometric mean fluorescence intensity (GeoMFI) of DCF relative to the control group (set as 1.0), as measured by flow cytometry. (G) Intracellular GSH and (H) MDA levels (n = 3). $^{**}p < 0.01$, $^{***}p < 0.001$, $^{****}p < 0.0001$. A *t*-test was used for comparisons between two groups. CYLD, cylindromatosis; ALP, Alkaline Phosphatase; WB, Western blotting; ROS, reactive oxygen species; DCF, dichlorofluorescein; GSH, reduced glutathione; MDA, malondialdehyde.

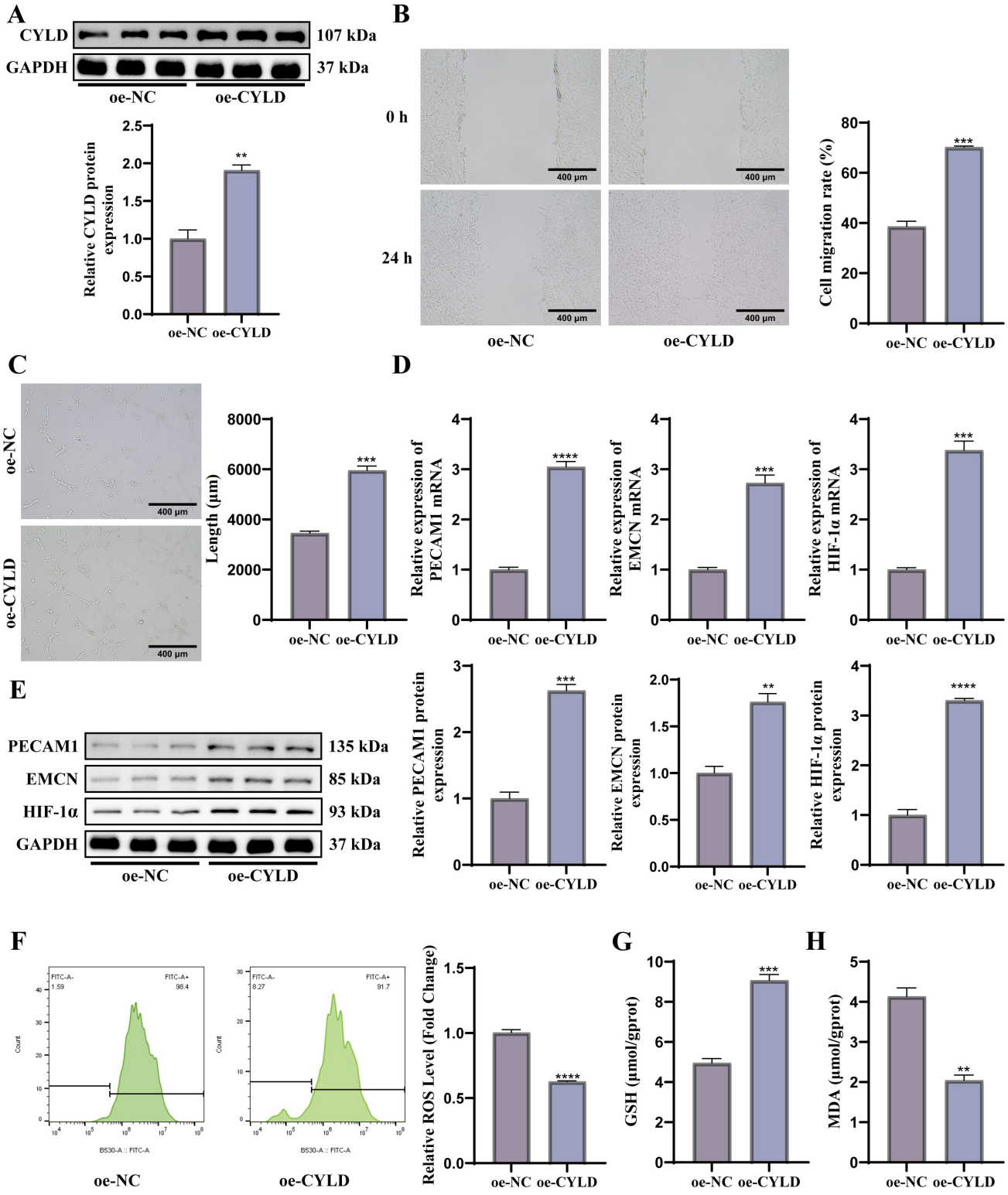


**Fig. 2. CYLD overexpression enhances angiogenic capacity in endothelial cells.** (A) WB of CYLD protein expression in bEnd.3 cells. (B) Cell migration ability assessed by scratch wound healing assay. (C) *In vitro* tube formation assay. (D,E) mRNA and protein expression levels of angiogenesis-related markers PECAM1, EMCN, and HIF-1$\alpha$ evaluated by RT-qPCR and WB. (F) Relative intracellular ROS level, determined as the fold change in geometric mean fluorescence intensity (GeoMFI) of DCF relative to the control group (set as 1.0), as measured by flow cytometry. (G) Intracellular GSH and (H) MDA levels (n = 3). $^{**}p < 0.01$, $^{***}p < 0.001$, $^{****}p < 0.0001$. A *t*-test was used for comparisons between two groups.

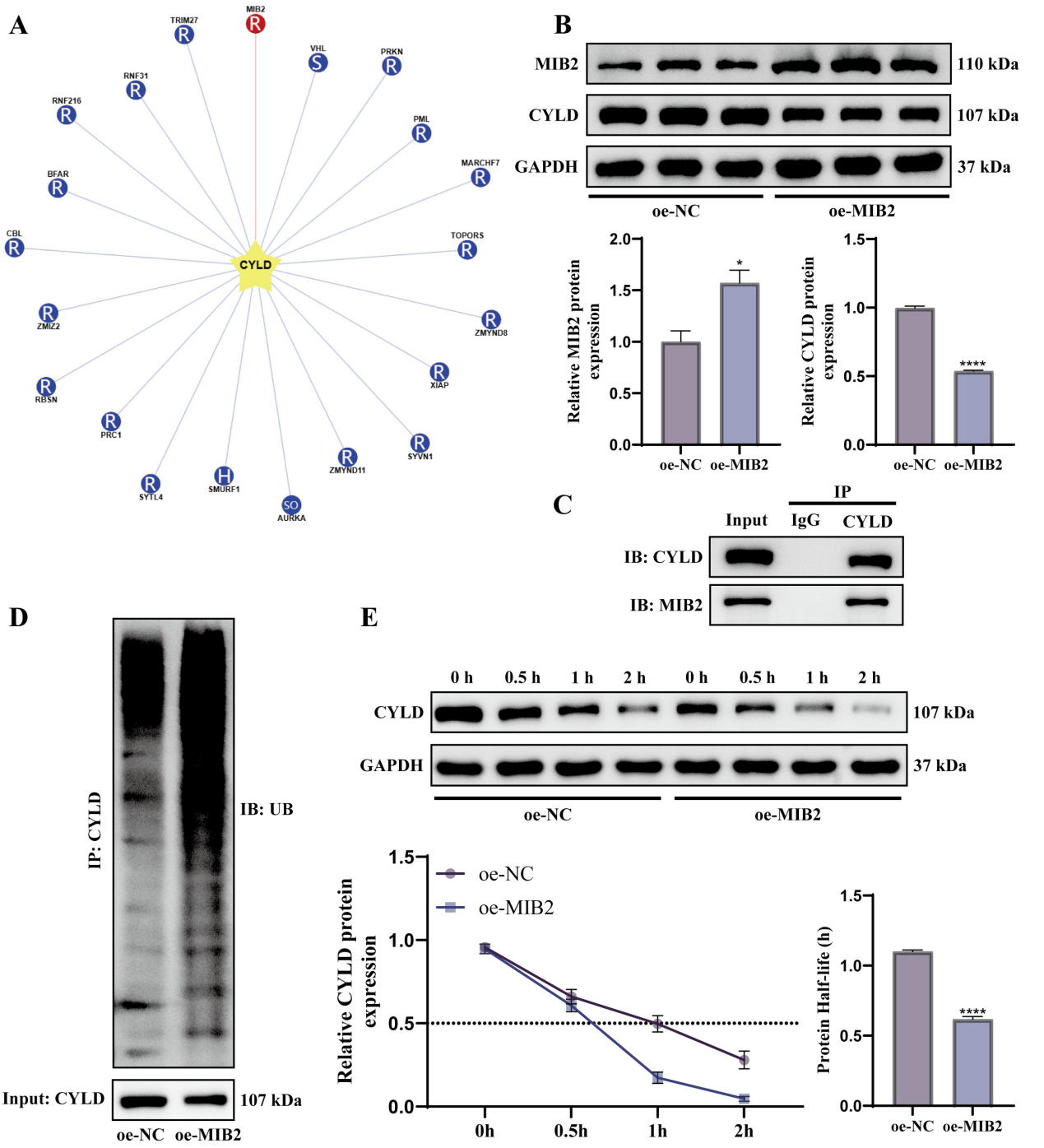


**Fig. 3. MIB2 functions as an E3 Ub ligase targeting CYLD for degradation.** (A) Schematic diagram from the UbiBrowser 2.0 database predicting MIB2 as a candidate E3 ubiquitin ligase for CYLD. (B) WB of CYLD protein levels in MC3T3-E1 cells after MIB2 overexpression. (C) Co-immunoprecipitation assay confirming the direct interaction between MIB2 and CYLD. (D) Ubiquitination assay showing the ubiquitination level of CYLD upon MIB2 overexpression. (E) CYLD protein stability assay using the protein synthesis inhibitor CHX (n = 3). *$p < 0.05$, ****$p < 0.0001$. A *t*-test was used for comparisons between two groups. For three or more groups, two-way analysis of variance (ANOVA) was applied, followed by Tukey's post hoc test. MIB2, Mind bomb 2; CHX, cycloheximide.

### *MIB2 Impairs Osteogenic Differentiation and Exacerbates Oxidative Stress by Degrading CYLD*

To determine whether MIB2 exerts its functional effects in osteoblasts by degrading CYLD, we performed rescue experiments in MC3T3-E1 cells. WB analysis showed that MIB2 overexpression significantly reduced CYLD protein levels ($p < 0.001$), while CYLD overexpression did not affect MIB2 expression (Fig. 4A). Subsequent functional assessment of osteogenic differentiation revealed that MIB2 overexpression markedly suppressed the differentia-

tion process, as indicated by reduced ALP activity, diminished mineralized nodule formation, and downregulated protein expression of the key osteogenic transcription factor Runx2. However, these inhibitory effects of MIB2 on osteogenic differentiation were substantially reversed by concomitant overexpression of CYLD ($p < 0.01$, Fig. 4B–D). Regarding oxidative stress, MIB2 overexpression led to a significant increase in intracellular ROS and MDA levels, concurrently with a decrease in GSH ($P < 0.0001$). Similarly, restoring CYLD expression effectively counteracted the oxidative stress induced by MIB2 overexpression ($p < 0.05$, Fig. 4E–G). Together, these results demonstrate that MIB2 inhibits osteogenic differentiation and aggravates oxidative stress primarily by promoting the degradation of CYLD.

### *The MIB2-CYLD Axis in Osteoblasts Disrupts Endothelial Function via Oxidative Stress*

To simulate the physiological interaction between osteoblasts and endothelial cells, we established a non-contact Transwell co-culture system. After co-culturing bEnd.3 endothelial cells with MC3T3-E1 cells that had been subjected to MIB2 and CYLD overexpression, we assessed the functionality of the endothelial cells in the lower chambers. WB analysis confirmed that MIB2 was successfully overexpressed in the co-cultured MC3T3-E1 osteoblasts ($p < 0.0001$), while CYLD protein levels were significantly suppressed by MIB2 overexpression ($p < 0.0001$). This suppression of CYLD was effectively rescued by concomitant CYLD overexpression ($p < 0.001$, Fig. 5A). Subsequently, the results demonstrated that MIB2 upregulation in osteoblasts suppressed the expression of angiogenesis markers (PECAM1, EMCN, and HIF-1$\alpha$) in endothelial cells, while concurrently promoting intracellular ROS accumulation. Conversely, CYLD upregulation effectively reversed these effects induced by MIB2 overexpression ($p < 0.0001$, Fig. 5B–D). Analysis of the conditioned medium further revealed that CYLD restoration in osteoblasts significantly rescued the oxidative stress caused by MIB2 overexpression, evidenced by elevated MDA and reduced GSH levels ($p < 0.001$, Fig. 5E,F). These findings indicate that the MIB2-CYLD regulatory axis in osteoblasts plays a pivotal role in osteogenic-angiogenic coupling, primarily by modulating the oxidative stress microenvironment.

## Discussion

This study provides significant conceptual and mechanistic insights into osteogenic-angiogenic coupling by systematically characterizing the MIB2-CYLD axis. We identified CYLD as a key promoter of osteogenic differentiation, angiogenesis, and redox homeostasis. Furthermore, we discovered that MIB2 acts as a specific E3 Ub ligase for CYLD, promoting its degradation. Disruption of this axis in osteoblasts impaired endothelial function via secretory oxidative stress, revealing a transcellular mechanism that links metabolic bone disease and vascular dysfunction.

Our findings consolidate and extend previous hints of CYLD's role in skeletal and vascular biology. While earlier studies in CYLD-deficient models implicated it in bone formation and angiogenesis through pathways such as TGF-$\beta$ and NF-$\kappa$B [26–28], its specific function within osteogenic-angiogenic coupling remained undefined. Here, we demonstrated that CYLD overexpression enhanced osteogenic markers (ALP, Runx2, mineralization) in MC3T3-E1 cells and angiogenic capacity (migration, tube formation, PECAM1, EMCN, HIF-1$\alpha$) in bEnd.3 cells. Crucially, we positioned CYLD as a homeostatic regulator of oxidative stress within this coupling, as its overexpression reduced intracellular ROS and MDA levels while increasing GSH in both cell types. This suggests that CYLD may target oxidative stress-related signaling molecules, such as NADPH oxidase 4 (Nox4) and NF-$\kappa$B p65, via its deubiquitinase activity [29,30], thereby maintaining a permissive redox environment for both osteogenesis and angiogenesis.

MIB2, an E3 Ub ligase, has known roles in embryonic development and cancer progression through substrates such as Notch and TGF-$\beta$ receptors [31], but its interaction with CYLD or role in bone metabolism was unexplored. Our co-IP and ubiquitination assays confirmed that MIB2 directly binds CYLD and promotes its ubiquitination and proteasomal degradation, consistent with proteomic data identifying MIB2 as a CYLD-interacting protein [32]. Additionally, a previous report indicated that MIB2 enhanced NF-$\kappa$B signaling in inflammation by promoting Ub-dependent CYLD degradation [33]. Our finding newly connects MIB2 to bone metabolism by targeting CYLD, establishing a foundation for investigating its role in skeletal disorders.

Rescue experiments confirmed the CYLD-dependence of MIB2's effects on osteoblast function. MIB2 overexpression suppressed osteogenic differentiation and induced oxidative stress, while co-transduction with oe-CYLD reversed these phenotypes. We proposed a model where, physiologically, CYLD suppresses ROS-generating signaling molecules to maintain redox balance via its deubiquitinase activity, thereby promoting osteogenesis [34]. When MIB2 is upregulated, it degrades CYLD, lifting this inhibition and causing ROS overaccumulation. Excessive ROS directly damages osteoblasts and inhibits differentiation via pathways like p38 MAPK [35,36]. Thus, the MIB2-CYLD axis acts as a critical molecular switch for oxidative stress in regulating osteogenesis.

The core of osteogenic-angiogenic coupling lies in the bidirectional communication between osteoblasts and endothelial cells via paracrine signals [37]. Using a Transwell co-culture system, we demonstrated that MIB2 overexpression in osteoblasts suppressed endothelial angiogenic markers PECAM1, EMCN, and HIF-1$\alpha$ and increased ROS in endothelial cells by secreted factors, effects rescued by

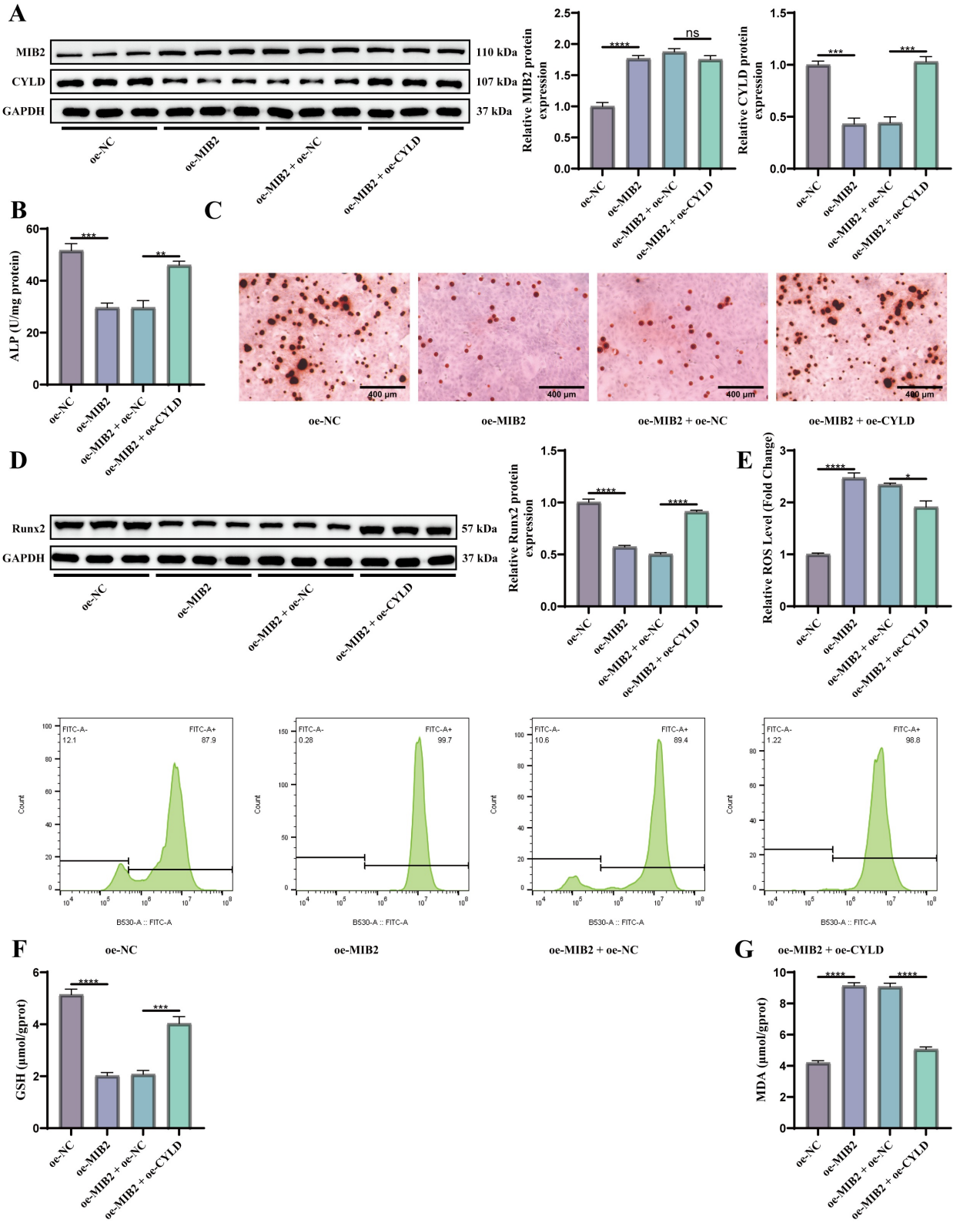


**Fig. 4. MIB2 impairs osteogenic differentiation and exacerbates oxidative stress by degrading CYLD.** (A) WB of MIB2 and CYLD protein expression. (B) ALP activity assay. (C) Alizarin Red S staining of mineralized nodules. (D) WB of Runx2 protein expression. (E) Relative intracellular ROS level, determined as the fold change in geometric mean fluorescence intensity (GeoMFI) of DCF relative to the control group (set as 1.0), as measured by flow cytometry. (F) Intracellular GSH and (G) MDA levels (n = 3). ns $p > 0.05$, *$p < 0.05$, **$p < 0.01$, ***$p < 0.001$, ****$p < 0.0001$. For three or more groups, one-way analysis of variance (ANOVA) was applied, followed by Tukey's post hoc test.

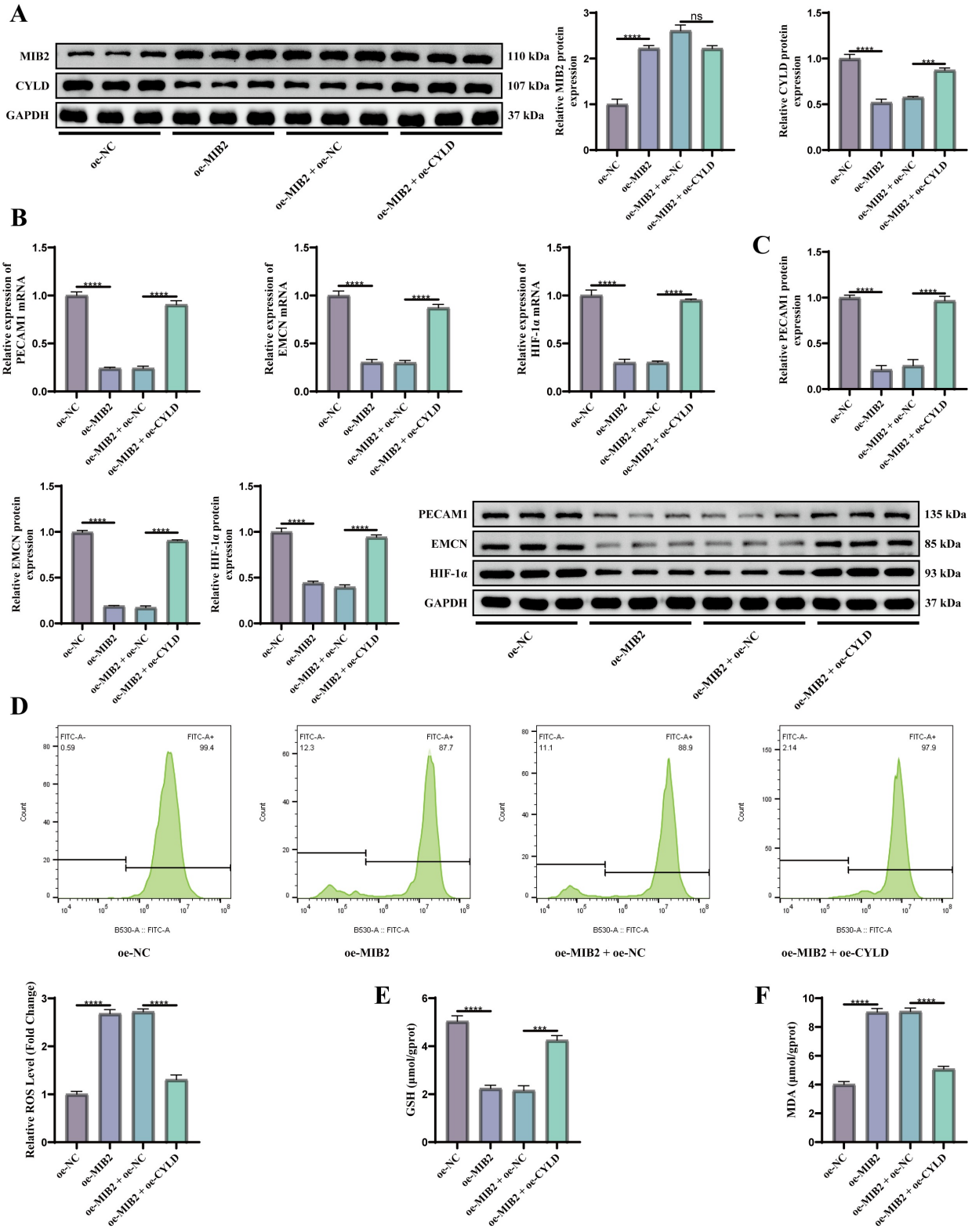


**Fig. 5. The MIB2-CYLD axis in osteoblasts disrupts endothelial function via oxidative stress.** (A) WB analysis of MIB2 and CYLD protein levels in MC3T3-E1 osteoblasts. (B,C) mRNA and protein expression levels of angiogenesis-related markers (PECAM1, EMCN, HIF-1$\alpha$) in bEnd.3 cells evaluated by (B) RT-qPCR and (C) WB. (D) Relative intracellular ROS levels in bEnd.3 cells, determined as the fold change in geometric mean fluorescence intensity (GeoMFI) of DCF relative to the control group (set as 1.0), as measured by flow cytometry. (E,F) Measurement of (E) GSH and (F) MDA levels in the conditioned medium from the co-culture system (n = 3). ns $p > 0.05$, ***$p < 0.001$, ****$p < 0.0001$. For three or more groups, one-way analysis of variance (ANOVA) was applied, followed by Tukey's post hoc test.

CYLD restoration. Analysis of the conditioned medium confirmed that disruption of the osteoblastic MIB2-CYLD axis elevates secretory oxidative stress factors, such as lipid peroxides and IL-6. These can directly damage endothelial tight junctions and inhibit VEGF-mediated tubulogenesis [38,39], thereby disrupting osteogenic-angiogenic coupling. This finding newly establishes the osteoblastic MIB2-CYLD axis as a bridge connecting osteogenesis and angiogenesis.

While our study focuses on MIB2 as an upstream regulator of CYLD, understanding the regulators of MIB2 itself is crucial for contextualizing this axis within broader signaling networks. Given this limitation, several plausible upstream mechanisms can be hypothesized based on MIB2's biology. MIB2 is known to be regulated by post-translational modifications. For instance, MIB2 can be phosphorylated by kinases such as CaMKII$\beta$, which influences its stability and E3 ligase activity towards other substrates [40]. Furthermore, inflammatory cytokines like tumor necrosis factor-$\alpha$ and TGF-$\beta$, which are often dysregulated in OP, can transcriptionally upregulate MIB2 expression in other cellular contexts [41,42]. It is therefore conceivable that in the bone microenvironment, mechanical unloading, hormonal changes (e.g., estrogen deficiency), or pro-inflammatory signals could serve as the initial triggers that elevate MIB2 expression or activity, thereby initiating the pathogenic cascade of CYLD degradation, oxidative stress, and uncoupling. Future work will prioritize the screening and validation of these and other upstream regulators to complete the comprehensive signaling network governing the MIB2-CYLD axis.

Current pharmacological interventions for OP, such as bisphosphonates and parathyroid hormone analogs, primarily modulate bone resorption or formation, with limited efficacy on intraosseous vascularization [43,44]. In contrast, the MIB2-CYLD axis concurrently regulates osteogenesis, angiogenesis, and their shared pathological mechanism (oxidative stress), exhibiting superior multi-target therapeutic potential. Our findings highlight this axis as a promising target for novel therapeutic strategies. The growing field of ubiquitination-targeted therapies, particularly proteolysis-targeting chimeras and small-molecule inhibitors of E3 ligases, provides a compelling framework [45,46]. Specifically, developing MIB2-specific small-molecule inhibitors that target its HECT Ub ligase domain could prevent CYLD degradation, thereby restoring its protective functions. Alternatively, other complementary strategies would focus on stabilizing CYLD, either by inhibiting kinases that prime it for ubiquitination (e.g., IKK$\epsilon$/TBK1-mediated phosphorylation) or using molecular glues to enhance its stability [47,48]. These strategies align with recent advances in targeting the UPS for skeletal disorders, such as the development of SMURF1 inhibitors to promote bone formation [49]. By simultaneously achieving antioxidant, pro-osteogenic, and pro-angiogenic effects, targeting the MIB2-CYLD axis could address the multifaceted pathology of OP and other complex skeletal disorders where vascular compromise is a key feature, paving the way for more effective and holistic treatments.

This study still has several limitations. First, the murine cell-based Transwell co-culture system cannot fully recapitulate the complex *in vivo* bone microenvironment. Subsequent studies will establish 3D organoid models incorporating osteoblasts, endothelial cells, and osteoclasts to more accurately validate the functional role of the MIB2-CYLD axis. Second, the *in vivo* regulatory significance remains unverified. Future investigations should generate osteoblast-specific MIB2 knockout or CYLD overexpression mouse models, combined with OVX-induced OP models, to systematically evaluate the axis's regulation of bone mass and intraosseous vascular density in living organisms. Concurrently, we will analyze MIB2 and CYLD expression in bone tissue samples from OP patients to examine their correlation with clinical parameters of bone density and vascularity.

## Conclusion

Our study reveals that MIB2 impairs osteogenic-angiogenic coupling by promoting the Ub-mediated degradation of CYLD, thereby disrupting redox homeostasis in osteoblasts and endothelial cells. This discovery deepens the understanding of the skeletal metabolic microenvironment and lays a critical foundation for developing novel therapeutic strategies targeting the MIB2/CYLD axis, aiming to simultaneously ameliorate oxidative stress, bone loss, and impaired vascularization.

## Availability of Data and Materials

The datasets used and analyzed during the current study are available from the corresponding author on reasonable request.

## Author Contributions

CS: Conceptualization, Formal analysis, Methodology, Visualization, Writing — Original draft and Writing — Critical revision and Editing; XX: Data curation, Validation, and Writing — Critical revision and Editing; YX: Data curation, Investigation, and Writing — Critical revision and Editing; LP: Formal analysis, Investigation, and Writing — Critical revision and Editing; ZA: Investigation and Writing — Critical revision and Editing; RL: Methodology, Software, and Writing — Critical revision and Editing; YC: Resources, Validation and Writing — Critical revision and Editing; JL: Conceptualization, Project administration, Resources, Supervision and Writing — Critical revision and Editing. All authors have given final approval of the version to be published; have agreed on the journal to which the article has been submitted; and have agreed to be accountable for all aspects of the work.

## Ethics Approval and Consent to Participate

Not applicable.


## Acknowledgment

Not applicable.

## Funding

This research received no external funding.


## Conflict of Interest

The authors declare no conflict of interest.

## Supplementary Material

Supplementary material associated with this article can be found, in the online version, at https://doi.org/10.24976/Discov.Med.202638204.17.

## References


[1] Salhotra A, Shah HN, Levi B, Longaker MT. Mechanisms of bone development and repair. Nature Reviews. Molecular Cell Biology. 2020; 21: 696–711. https://doi.org/10.1038/s41580-020-00279-w.

[2] Clézardin P, Coleman R, Puppo M, Ottewell P, Bonnelye E, Paycha F, *et al*. Bone metastasis: mechanisms, therapies, and biomarkers. Physiological Reviews. 2021; 101: 797–855. https://doi.org/10.1152/physrev.00012.2019.

[3] Yang Q, Liu S, Liu H, Liu Y, He Z, Zheng Z, *et al*. A new paradigm in bone tissue biomaterials: Enhanced osteogenesis-angiogenic coupling by targeting H-type blood vessels. Biomaterials. 2026; 324: 123423. https://doi.org/10.1016/j.biomaterials.2025.123423.

[4] Su Z, Liu J, Zheng Z, Zhen L, Hu X, Luo D. Recent advances in the crosstalk between bone and vascular system: from mechanism to therapy. Cellular Signalling. 2025; 135: 112001. https://doi.org/10.1016/j.cellsig.2025.112001.

[5] Qin Q, Lee S, Patel N, Walden K, Gomez-Salazar M, Levi B, *et al*. Neurovascular coupling in bone regeneration. Experimental & Molecular Medicine. 2022; 54: 1844–1849. https://doi.org/10.1038/s12276-022-00899-6.

[6] Bal Z, Takakura N. Hydrogel Use in Osteonecrosis of the Femoral Head. Gels (Basel, Switzerland). 2024; 10: 544. https://doi.org/10.3390/gels10080544.

[7] Hu W, Si Y, Xie X, Xu J. Research Progress on Icariin Promoting Bone Injury Repair and Regeneration. Pharmaceuticals (Basel, Switzerland). 2025; 18: 1174. https://doi.org/10.3390/ph18081174.

[8] Zhang C, Li H, Li J, Hu J, Yang K, Tao L. Oxidative stress: A common pathological state in a high-risk population for osteoporosis. Biomedicine & Pharmacotherapy. 2023; 163: 114834. https://doi.org/10.1016/j.biopha.2023.114834.

[9] Sheppard AJ, Barfield AM, Barton S, Dong Y. Understanding Reactive Oxygen Species in Bone Regeneration: A Glance at Potential Therapeutics and Bioengineering Applications. Frontiers in Bioengineering and Biotechnology. 2022; 10: 836764. https://doi.org/10.3389/fbioe.2022.836764.

[10] Yang K, Cao F, Xue Y, Tao L, Zhu Y. Three Classes of Antioxidant Defense Systems and the Development of Postmenopausal Osteoporosis. Frontiers in Physiology. 2022; 13: 840293. https://doi.org/10.3389/fphys.2022.840293.

[11] Nappi F, Fiore A, Masiglat J, Cavuoti T, Romandini M, Nappi P, *et al*. Endothelium-Derived Relaxing Factors and Endothelial Function: A Systematic Review. Biomedicines. 2022; 10: 2884. https://doi.org/10.3390/biomedicines10112884.

[12] Tao ZS, Shen CL. Favorable osteogenic activity of vericiguat doped in $\beta$-tricalcium phosphate: In vitro and in vivo studies. Journal of Biomaterials Applications. 2024; 38: 1073–1086. https://doi.org/10.1177/08853282241245543.

[13] Mathien S, Tesnière C, Meloche S. Regulation of Mitogen-Activated Protein Kinase Signaling Pathways by the Ubiquitin-Proteasome System and Its Pharmacological Potential. Pharmacological Reviews. 2021; 73: 263–296. https://doi.org/10.1124/pharmrev.120.000170.

[14] Dong Y, Chen Y, Ma G, Cao H. The role of E3 ubiquitin ligases in bone homeostasis and related diseases. Acta Pharmaceutica Sinica. B. 2023; 13: 3963–3987. https://doi.org/10.1016/j.apsb.2023.06.016.

[15] Qu J, Zou T, Lin Z. The Roles of the Ubiquitin-Proteasome System in the Endoplasmic Reticulum Stress Pathway. International Journal of Molecular Sciences. 2021; 22: 1526. https://doi.org/10.3390/ijms22041526.

[16] Kandel R, Jung J, Neal S. Proteotoxic stress and the ubiquitin proteasome system. Seminars in Cell & Developmental Biology. 2024; 156: 107–120. https://doi.org/10.1016/j.semcdb.2023.08.002.

[17] Huang Z, Tan Y. The Potential of Cylindromatosis (CYLD) as a Therapeutic Target in Oxidative Stress-Associated Pathologies: A Comprehensive Evaluation. International Journal of Molecular Sciences. 2023; 24: 8368. https://doi.org/10.3390/ijms24098368.

[18] Cao Y, Zhang X, Hu M, Yang S, Li X, Han R, *et al*. CYLD inhibits osteoclastogenesis to ameliorate alveolar bone loss in mice with periodontitis. Journal of Cellular Physiology. 2023; 238: 1036–1045. https://doi.org/10.1002/jcp.30990.

[19] Gao J, Sun L, Huo L, Liu M, Li D, Zhou J. CYLD regulates angiogenesis by mediating vascular endothelial cell migration. Blood. 2010; 115: 4130–4137. https://doi.org/10.1182/blood-2009-10-248526.

[20] Lin P, Lai X, Wu L, Liu W, Lin S, Ye J. Network analysis reveals important genes in human placenta. The Journal of Obstetrics and Gynaecology Research. 2021; 47: 2607–2615. https://doi.org/10.1111/jog.14820.

[21] Zheng W, Wang L, Geng S, Yang L, Lv X, Xin S, *et al*. CircMIB2 therapy can effectively treat pathogenic infection by encoding a novel protein. Cell Death & Disease. 2023; 14: 578. https://doi.org/10.1038/s41419-023-06105-3.

[22] Li R, Strilic B, Jin YJ, Shao J, Peng Y, Wang L, *et al*. The tumor suppressor FAT1 controls YAP/TAZ protein degradation and tumor cell proliferation through E3 ligase MIB2. PLoS ONE. 2025; 20: e0325535. https://doi.org/10.1371/journal.pone.0325535.

[23] Li R, Shao J, Jin YJ, Kawase H, Ong YT, Troidl K, *et al*. Endothelial FAT1 inhibits angiogenesis by controlling YAP/TAZ protein degradation via E3 ligase MIB2. Nature Communications. 2023; 14: 1980. https://doi.org/10.1038/s41467-023-37671-x.

[24] Wang X, Diao L, Sun D, Wang D, Zhu J, He Y, *et al*. OsteoporosAtlas: a human osteoporosis-related gene database. PeerJ. 2019; 7: 6778. https://doi.org/10.7717/peerj.6778.

[25] Fang Y, Li W, Dong C, Gao B, Guo W, Li M, *et al*. Inhibition of SLC40A1 represses osteoblast formation via inducing iron accumulation and activating the PERK/ATF4/CHOP pathway mediated oxidative stress. Redox Report: Communi-

cations in Free Radical Research. 2024; 29: 2428147. https://doi.org/10.1080/13510002.2024.2428147.

[26] Nguyen J, Massoumi R, Alliston T. CYLD, a mechanosensitive deubiquitinase, regulates TGF$\beta$ signaling in load-induced bone formation. Bone. 2020; 131: 115148. https://doi.org/10.1016/j.bone.2019.115148.

[27] Liu L, Jin R, Duan J, Yang L, Cai Z, Zhu W, *et al*. Bioactive iron oxide nanoparticles suppress osteoclastogenesis and ovariectomy-induced bone loss through regulating the TRAF6-p62-CYLD signaling complex. Acta Biomaterialia. 2020; 103: 281–292. https://doi.org/10.1016/j.actbio.2019.12.022.

[28] Zhao J, Wang X, Mi Z, Jiang X, Sun L, Zheng B, *et al*. STAT3/miR-135b/NF-κB axis confers aggressiveness and unfavorable prognosis in non-small-cell lung cancer. Cell Death & Disease. 2021; 12: 493. https://doi.org/10.1038/s41419-021-03773-x.

[29] Zhan Y, Xu D, Tian Y, Qu X, Sheng M, Lin Y, *et al*. Novel role of macrophage TXNIP-mediated CYLD-NRF2-OASL1 axis in stress-induced liver inflammation and cell death. JHEP Reports: Innovation in Hepatology. 2022; 4: 100532. https://doi.org/10.1016/j.jhepr.2022.100532.

[30] Fu YW, Li L, Wang XQ, Zhou Y, Zhu LF, Mei YM, *et al*. The inhibitory effect of the deubiquitinase cylindromatosis (CYLD) on inflammatory responses in human gingival fibroblasts. Oral Diseases. 2021; 27: 1487–1497. https://doi.org/10.1111/odi.13672.

[31] Nakabayashi O, Takahashi H, Moriwaki K, Komazawa-Sakon S, Ohtake F, Murai S, *et al*. MIND bomb 2 prevents RIPK1 kinase activity-dependent and -independent apoptosis through ubiquitylation of cFLIP$_L$. Communications Biology. 2021; 4: 80. https://doi.org/10.1038/s42003-020-01603-y.

[32] Rajan N, Elliott RJR, Smith A, Sinclair N, Swift S, Lord CJ, *et al*. The cylindromatosis gene product, CYLD, interacts with MIB2 to regulate notch signalling. Oncotarget. 2014; 5: 12126–12140. https://doi.org/10.18632/oncotarget.2573.

[33] Uematsu A, Kido K, Takahashi H, Takahashi C, Yanagihara Y, Saeki N, *et al*. The E3 ubiquitin ligase MIB2 enhances inflammation by degrading the deubiquitinating enzyme CYLD. The Journal of Biological Chemistry. 2019; 294: 14135–14148. https://doi.org/10.1074/jbc.RA119.010119.

[34] Jiang G, Cai Y, Cheng D, Wang H, Deng G, Xiang D. CYLD alleviates NLRP3 inflammasome-mediated pyroptosis in osteoporosis by deubiquitinating WNK1. Journal of Orthopaedic Surgery and Research. 2024; 19: 212. https://doi.org/10.1186/s13018-024-04675-2.

[35] Sun H, Xu J, Wang Y, Shen S, Xu X, Zhang L, *et al*. Bone microenvironment regulative hydrogels with ROS scavenging and prolonged oxygen-generating for enhancing bone repair. Bioactive Materials. 2023; 24: 477–496. https://doi.org/10.1016/j.bioactmat.2022.12.021.

[36] Li JC, Zhang DM, Xie J, Zhou XD. Co-Culturing of Osteoblasts and Chondrocytes Upregulates HIF-1 Pathway of Chondrocytes via MAPK Signaling. Sichuan Da Xue Xue Bao. Yi Xue Ban = Journal of Sichuan University. Medical Science Edition. 2022; 53: 92–97. https://doi.org/10.12182/20220160104. (In Chinese)

[37] Shen N, Maggio M, Woods I, C Lowry M, Almasri R, Gorgun C, *et al*. Mechanically activated mesenchymal-derived bone cells drive vessel formation via an extracellular vesicle mediated mechanism. Journal of Tissue Engineering. 2023; 14: 20417314231186918. https://doi.org/10.1177/20417314231186918.

[38] Arab HH, Abd El-Aal SA, Ashour AM, El-Sheikh AAK, Al Khabbaz HJ, Arafa ESA, *et al*. Targeting inflammation and redox perturbations by lisinopril mitigates Freund's adjuvant-induced arthritis in rats: role of JAK-2/STAT-3/RANKL axis, MMPs, and VEGF. Inflammopharmacology. 2022; 30: 1909–1926. https://doi.org/10.1007/s10787-022-00998-w.

[39] Zhang P, Fleming P, Andoniou CE, Waltner OG, Bhise SS, Martins JP, *et al*. IL-6-mediated endothelial injury impairs antiviral humoral immunity after bone marrow transplantation. The Journal of Clinical Investigation. 2024; 134: e174184. https://doi.org/10.1172/JCI174184.

[40] Zemoura K, Balakrishnan K, Grampp T, Benke D. $Ca^{2+}$/Calmodulin-Dependent Protein Kinase II (CaMKII) $\beta$-Dependent Phosphorylation of GABA$_{B1}$ Triggers Lysosomal Degradation of GABA$_B$ Receptors via Mind Bomb-2 (MIB2)-Mediated Lys-63-Linked Ubiquitination. Molecular Neurobiology. 2019; 56: 1293–1309. https://doi.org/10.1007/s12035-018-1142-5.

[41] Feltham R, Jamal K, Tenev T, Liccardi G, Jaco I, Domingues CM, *et al*. Mind Bomb Regulates Cell Death during TNF Signaling by Suppressing RIPK1's Cytotoxic Potential. Cell Reports. 2018; 23: 470–484. https://doi.org/10.1016/j.celrep.2018.03.054.

[42] Choi A, Nam SA, Kim WY, Park SH, Kim H, Yang CW, *et al*. Notch signaling in the collecting duct regulates renal tubulointerstitial fibrosis induced by unilateral ureteral obstruction in mice. The Korean Journal of Internal Medicine. 2018; 33: 774–782. https://doi.org/10.3904/kjim.2016.230.

[43] Cosman F, Langdahl B, Leder BZ. Treatment Sequence for Osteoporosis. Endocrine Practice: Official Journal of the American College of Endocrinology and the American Association of Clinical Endocrinologists. 2024; 30: 490–496. https://doi.org/10.1016/j.eprac.2024.01.014.

[44] Fuggle N, Rizzoli R, Beaudart C, Cortet B, Curtis EM, Hiligsmann M, *et al*. Parathyroid hormone receptor agonists in the management of osteoporosis. Nature Reviews. Rheumatology. 2025; 21: 599–611. https://doi.org/10.1038/s41584-025-01287-w.

[45] Li X, Song Y. Proteolysis-targeting chimera (PROTAC) for targeted protein degradation and cancer therapy. Journal of Hematology & Oncology. 2020; 13: 50. https://doi.org/10.1186/s13045-020-00885-3.

[46] Diehl CJ, Ciulli A. Discovery of small molecule ligands for the von Hippel-Lindau (VHL) E3 ligase and their use as inhibitors and PROTAC degraders. Chemical Society Reviews. 2022; 51: 8216–8257. https://doi.org/10.1039/d2cs00387b.

[47] Wegner J, Hunkler C, Ciupka K, Hartmann G, Schlee M. Increased IKKϵ protein stability ensures efficient type I interferon responses in conditions of TBK1 deficiency. Frontiers in Immunology. 2023; 14: 1073608. https://doi.org/10.3389/fimmu.2023.1073608.

[48] Domostegui A, Nieto-Barrado L, Perez-Lopez C, Mayor-Ruiz C. Chasing molecular glue degraders: screening approaches. Chemical Society Reviews. 2022; 51: 5498–5517. https://doi.org/10.1039/d2cs00197g.

[49] Tessier TM, Chowdhury A, Stekel Z, Fux J, Sartori MA, Teyra J, *et al*. Structural and functional validation of a highly specific Smurf2 inhibitor. Protein Science: a Publication of the Protein Society. 2024; 33: e4885. https://doi.org/10.1002/pro.4885.